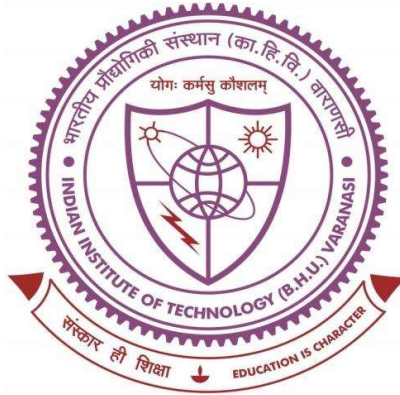


**Design and Optimization of Triply Periodic  
Minimal Surfaces based Porous Scaffolds for  
Bone Applications: A Conceptual Prosthetic  
Design for Restoration of Large Bone Defects**



**Thesis submitted in partial fulfillment  
for the Award of Degree**

**Doctor of Philosophy**

**by**

**Rati**

**SCHOOL OF BIOMEDICAL ENGINEERING  
INDIAN INSTITUTE OF TECHNOLOGY (BHU)  
(BANARAS HINDU UNIVERSITY)  
VARANASI – 221005, (U.P.), INDIA**

# CERTIFICATE

It is certified that the work contained in the thesis titled “**Design and Optimization of Triply Periodic Minimal Surfaces based Porous Scaffolds for Bone Applications: A Conceptual Prosthetic Design for Restoration of Large Bone Defects**” by “**Rati**” has been carried out under my supervision and this work has not been submitted elsewhere for a degree.

It is further certified that the student has fulfilled all the requirements of Comprehensive Examination, Candidacy and SOTA for the award of Ph.D. Degree.



**(Dr. Sanjay Kumar Rai)**  
**Supervisor**  
**Associate Professor,**  
**School of Biomedical Engineering,**  
**Indian Institute of Technology (BHU),**  
**Varanasi - 221005, (U.P.), India**

**SUPERVISOR**

## DECLARATION BY THE CANDIDATE

I, **Rati**, certify that the work embodied in this Ph.D. thesis is my own bona fide work and carried out by me under the supervision of **Dr. Sanjay Kumar Rai** from **21<sup>st</sup> July 2015 to 30<sup>th</sup> June 2022** at the School of Biomedical Engineering, Indian Institute of Technology (BHU), Varanasi. The matter embodied in this thesis has not been submitted for the award of any other degree/diploma.

I declare that I have faithfully acknowledged and given credits to the research workers wherever their work has been cited in my work in this thesis. I further declare that I have not wilfully copied any other's work, paragraphs, text, data, results, etc., reported in journals, books, magazines, reports dissertations, theses, etc., or available at websites and have not included them in this thesis and have not cited as my own work.

Date: 30/06/2022

Place: Varanasi

*Rati*

Signature of the Student  
(Rati)

## CERTIFICATE BY THE SUPERVISOR

It is certified that the above statement made by the student is correct to the best of our knowledge.

*Sanjay Kumar Rai*

(Dr. Sanjay Kumar Rai)  
Supervisor

Associate Professor,  
School of Biomedical Engineering,  
Indian Institute of Technology (BHU),  
Varanasi - 221005, (U.P.), India

SUPERVISOR

*Sanjeev Kumar Mahto* 30.06.22

(Dr. Sanjeev Kumar Mahto)  
Coordinator

Associate Professor  
School of Biomedical Engineering,  
Indian Institute of Technology (BHU),  
Varanasi - 221005, (U.P.), India

समन्वयक/CO-ORDINATOR  
जैव चिकित्सा अभियांत्रिकी स्कूल  
SCHOOL OF BIOMEDICAL ENGG.  
भारतीय प्रौद्योगिकी संस्थान (का.हि.वि.)  
INDIAN INSTITUTE OF TECHNOLOGY (B.H.U.)  
वाराणसी-221005/ARANASI-221005

## COPYRIGHT TRANSFER CERTIFICATE

**Title of the Thesis:** Design and Optimization of Triply Periodic Minimal Surfaces based Porous Scaffolds for Bone Applications: A Conceptual Prosthetic Design for Restoration of Large Bone Defects

**Name of the Student:** Rati

### Copyright Transfer

The undersigned hereby assigns to the Indian Institute of Technology (BHU), Varanasi all rights under copyright that may exist in and for the above thesis submitted for the award of the Doctor of Philosophy.

**Date:** 30/06/2022

**Place:** Varanasi

*Rati*

**Signature of the Student  
(Rati)**

**Note:** However, the author may reproduce or authorize others to reproduce material extracted verbatim from the thesis or derivative of the thesis for author's personal use provided that the source and the Institute's copyright notice are indicated.

## *ACKNOWLEDGEMENTS*

---

It is my greatest pleasure to have this opportunity to express my sincere appreciation to everyone who helped me during my Ph.D. program at the Indian Institute of Technology (Banaras Hindu University), Varanasi. First, I want to thank my supervisor Dr. Sanjay Kumar Rai, for his valuable guidance, encouragement, and paternal behavior throughout the work. His inspiring and excellent guidance is the key reason that I could successfully finish each of the research objectives. Without his guidance as a great mentor, this work would not have been possible.

A very special thanks to my external advisor Prof. Dr. Shekhar Madhukar Kumta (expert- Orthopedics, and Traumatology, CUHK, Hong Kong) for guiding me at each and every step throughout my thesis and beyond. My words will never be enough to thank you for your immense support, guidance, and trust in my work.

I offer my special thanks to Dr. Sanjeev Kumar Mahto, Coordinator of the School of Biomedical Engineering for providing all the necessary facilities for the School. I would like to express my appreciation to my research progress evaluation committee (RPEC) members, Dr. S.K. Mahto and Prof. S.K. Panda, for their kind cooperation during the course of my work.

I would like to thank the Institute of Medical Sciences, Banaras Hindu University, for providing the necessary data, without which the completion of this work was not possible. I also wish to express thankfulness to all other respected faculty members of the School for their kind support and valuable suggestions. I would like to sincerely thank all the supporting staff of the School for their kind help whenever I required it.

I would like to thank my wonderful lab mates and juniors for their stimulating discussions and for creating a cheerful environment in the lab. I would also like to thank my batch mates and friends for their extended support. This thesis would not have been possible

without their cooperation. I thank all my beloved friends across the globe for sharing my happy and sorrowful moments at all times.

I can never forget my parents Mr. Shobh Nath & Mrs. Chandrwati, my In-laws Dr. Nehru Singh & Dr. Kalawati, my (late) brother Mr. Mahendra Pratap, brother in law Mr. K.S Mohan, sisters Archana and Vandana, sister in law Dr. Pooja Singh, whose boundless love, constant inspiration, emotional support, and blessings have provided me encouragement at every step of life. My parents' everlasting shower of blessings kept me moving easily with all hazards vanishing miraculously. I am especially thankful to my husband Dr. Nishant Singh whose consistent guidance, support, and love throughout this journey made this dream come true. My word power fails to express my feelings of gratitude to my loving son Ridant for his unconditional love and sacrifice during my work.

Lastly, I would like to thank Almighty, for having made everything possible by giving me the strength and courage to do this work.

**Date: 30/06/2022**

**Place: Varanasi**

A handwritten signature in blue ink that reads "Rati" with a small flourish at the end.

**(Rati)**

***Dedicated  
To  
My Loving Family***

# Table of Contents

Page No.

<b>List of figures</b> .....	<b>xiii-xix</b>
<b>List of tables</b> .....	<b>xx-xxi</b>
<b>Preface</b> .....	<b>xxii-xxvi</b>
<b>Chapter 1</b>	
<b>Introduction</b> .....	<b>01-10</b>
1.1 The clinical impact of Patient Specific Implants (PSI) and the requirement of porous structures	02
1.2 Modelling porous PSI: Role of multiple parameters .....	05
1.3 Purpose of study: Motivation.....	07
1.4 Research problem: Gap.....	07
1.5 Research objectives: Aim and Contributions.....	08
1.6 Novel Aspects of the Proposed Work.....	09
1.7 Thesis structure .....	10
<b>Chapter 2</b>	
<b>Literature Review</b> .....	<b>11-64</b>
2.1 Bone tissue .....	12
2.1.1 Bone structure and composition.....	12
2.1.2 Bone cells .....	14
2.1.3 Bone growth and modelling .....	15
2.1.4 Mechanical Properties of Human Bone .....	16
2.2 Bone situations needing repair.....	19
2.2.1 Fractures .....	21
2.2.2 Segmental Bone defects .....	22
2.3 Large segmental bone defects (LSBD).....	23
2.3.1 Definition .....	24
2.3.2 Size matters .....	26
2.3.3 Causes.....	26
2.3.4 Reconstruction alternatives .....	27
2.4 Post-operative complications associated with metal implants.....	32
2.4.1 Mechanical Complications.....	33
2.4.1.1 Stress shielding .....	33

2.4.1.2 Interface failure .....	34
2.4.2 Drawbacks of solid implants .....	34
2.4.3 Current approaches to avoid stress shielding .....	35
2.5 Need of porous structures for the treatment of LSBDD .....	37
2.5.1 Introduction to Porous structures .....	37
2.5.2 Advantages of Porous structures in implant applications .....	41
2.5.3 Types of porous structures .....	43
2.6 Triply periodic minimal surfaces (TPMS).....	48
2.6.1 What are TPMS structures .....	48
2.6.2 Family of TPMS.....	50
2.6.3 TPMS as porous scaffolds for implant applications .....	52
2.7 Fabrication of porous scaffolds for orthopaedic applications.....	53
2.7.1 Conventional Manufacturing Methods .....	54
2.7.2 Additive Bio-manufacturing Technology .....	54
2.8 Biocompatibility of Titanium and its alloys for porous scaffolds .....	57
2.8.1 Titanium versus other alloys .....	58
2.8.2 Advantages of Ti6Al4V .....	59
2.9 Predicting the behaviour of porous materials with FEA.....	61
2.9.1 Structural analysis to study the mechanical behaviour .....	62
2.9.2 Permeability analysis .....	63
<b>Chapter 3</b>	
<b>Mathematical Modeling and Design of TPMS Porous Structures .....</b>	<b>65-100</b>
3.1 Introduction.....	66
3.2 TPMS unit cell Investigation and selection criteria.....	66
3.3 Modelling approaches of TPMS .....	69
3.3.1 Analytical methods.....	70
3.3.2 Finite element-based methods.....	71
3.4 Mathematical representation of TPMS .....	73
3.4.1 Parameterization of TPMS structures .....	73
3.4.1.1 The Gauss map.....	73
3.4.1.2 Stereographic Projection .....	74
3.4.2 Mathematical equations of TPMS.....	76

3.4.3 Surface Triangulation of TPMS .....	77
3.4.4 Bilayer surface generation .....	79
3.4.5 Capping parallel layers.....	80
3.5 Code implementation and TPMS UNIT CELL Generation .....	81
3.5.1 Role of level set constant ‘c’ .....	82
3.5.2 UNIT Cell generation.....	84
3.6 Optimization and modification of unit cells .....	85
3.7 Conversion of STL unit cell to the solid models .....	86
3.7.1 Brief introduction to NURBS surface generation .....	89
3.7.2 Freeform resurfacing of TPMS unit cells.....	91
3.8 TPMS Unit cell shape and size identification.....	94
3.9 Finite number of unit cells in a lattice for finite element studies.....	97
3.10 Unit cell and lattice cell representation for developing PS porous scaffold.....	99
<b>Chapter 4</b>	
<b>Morphological Analysis of TPMS Scaffolds.....</b>	<b>101-115</b>
4.1 Introduction.....	102
4.2 Morphological estimations.....	104
4.2.1 Porosity.....	104
4.2.2 Pore size .....	104
4.2.3 Thickness.....	105
4.2.4 Surface-Area-to-Volume ratio (SA/Vp).....	107
4.3 Summary.....	108
<b>Chapter 5</b>	
<b>Mechanical Performance Evaluation of TPMS Scaffolds for Bone Applications .....</b>	<b>116-134</b>
5.1 Introduction.....	117
5.2 FEA simulations of lattice structures.....	118
5.2.1 Lattice structure dimensions .....	118
5.2.2 Material Properties used.....	119
5.2.3 Mesh preparation and element technology .....	119
5.2.4 Loading and boundary conditions .....	121
5.2.5 Measurement of mechanical properties.....	122
5.2.6 Mechanical Results and discussions for High Porosity Lattice Structures .....	123

5.2.6.1 Deformation behaviour of lattice structures.....	123
5.2.6.2 Stress-strain behaviour .....	124
5.2.6.3 Effective elastic modulus ( $E_{\text{eff}}$ ).....	125
5.2.6.4 Compressive strength.....	127
5.2.7 Mechanical Results and discussions for Lattice Structures having porosity ranging from 50% to 80%. .....	128
5.2.7.1 Deformation behaviour of lattice structures.....	128
5.2.7.2 Stress-strain behaviour .....	129
5.2.7.3 Effective elastic modulus ( $E_{\text{eff}}$ ).....	130
5.2.7.4 Compressive strength .....	132
5.3 Summary .....	132
<b>Chapter 6</b>	
<b>Fluid Flow Analysis of TPMS Unit Cells .....</b>	<b>135-155</b>
6.1 Introduction to behaviour of porous cells in tissue engineering application .....	136
6.2 Problem Definition.....	137
6.3 TPMS unit cell fluidic behaviour simulation.....	139
6.4 Boundary conditions and Governing equations in CFD analysis .....	141
6.5 Convergence and Solutions.....	143
6.6 Fluid flow mechanism of porous scaffolds.....	143
6.7 Results and Discussion .....	147
6.8 Permeability .....	151
6.9 Summary .....	154
<b>Chapter 7</b>	
<b>Functionality Assessment of Scaffold under Biomechanical Loading .....</b>	<b>156-184</b>
7.1 Introduction.....	157
7.2 Image acquisition .....	160
7.2.1 Preparing the acquired CT Data .....	164
7.2.1.1 Windowing.....	164
7.2.1.2 Volume Rendering .....	165
7.2.2 Extraction of material properties from CT data .....	166
7.3 Segmentation and 3D reconstruction of femur bone .....	166
7.3.1 Automatic segmentation.....	167
7.3.1.1 Threshold .....	167

7.3.1.2 Region Growing .....	169
7.3.2 Manual segmentation (Edit mask) .....	170
7.4 Calculate 3D.....	171
7.5 Smoothing .....	173
7.6 Optimization .....	173
7.7 Surgical simulation of patient specific scaffold.....	174
7.8 Boolean intersection of porous structure on the solids .....	174
7.9 Designing exterior and interior geometry to achieve anatomical compatibility.....	175
7.10 Simulation Protocol .....	177
7.11 Functionality Assessment of Scaffold under Biomechanical Loading .....	180
7.12 Summary .....	184

## **Chapter 8**

### **Development of Patient-Specific Scaffold and Prosthesis (Morphologically Controlled) for Large Bone Defects .....**

<b>185-192</b>	
8.1 Introduction.....	186
8.2 Virtual treatment protocol and rationale .....	186
8.2.1 Development of conceptual patient specific implant to treat tumorized femur bone .....	188
8.2.2 Pore mapping on patient specific implant.....	189
8.3 Summary .....	191
Conclusions and Recommendations for Future Work .....	193-196
References .....	197-215
APPENDIX.....	216-219
Permission from Central Ethical Committee .....	220
Publications.....	221-222

## LIST OF FIGURES

<b>Figure No.</b>	<b>Figure Description</b>	<b>Page No.</b>
<b>Figure 1.1</b>	Variations in human populations and their respective femur bone anatomy.	03
<b>Figure 1.2</b>	Parameters affecting the mechanical and biological responses of a porous implant.	06
<b>Figure 1.3</b>	Structure of Thesis.	10
<b>Figure 2.1</b>	Hierarchical structure of bone ranging from macro to sub-nanostructure scale (Mullen et al. 2010).	13
<b>Figure 2.2</b>	Bone remodeling process (from Servier medical art)	16
<b>Figure 2.3</b>	Stress-strain curve of cortical bone loaded at various strain rates (Novitskaya et al. 2011).	17
<b>Figure 2.4</b>	Stress-strain curve of trabecular bone for different relative density (Shim et al. 2012).	18
<b>Figure 2.5</b>	Variation of Young's modulus with density of human bone (Gibson et al. 2010).	19
<b>Figure 2.6</b>	Skeletal defects are treated with prosthetic implants. (a) Examples of skeletal tissues with major risk of injuries and defects (Loebel and Burdick 2018). (b) Orthopaedic implants used to treat bone defects. (Garot et al. 2021).	20
<b>Figure 2.7</b>	Different types of bone fractures (Edition, T.E., 2014).	21
<b>Figure 2.8</b>	Bone fracture healing (Anastasio et al. 2021).	22
<b>Figure 2.9</b>	3D model of human femur bone showing a) Intact femur b) segmental bone defect (Bosiakov et al. 2017).	23
<b>Figure 2.10</b>	Categories of segmental bone defects. A: Limited defect; B: Bone fragments have contact; C: Bone fragments have no contact (segmental defect); D: Complete articular defect. (Solomin and Slongo 2016).	24
<b>Figure 2.11</b>	Classification of bone defects on the basis of defect site and size (Solomin and Slongo 2016).	25
<b>Figure 2.12</b>	Causes of Bone loss. (Zhou et al. 2021).	27
<b>Figure 2.13</b>	Current biological bone reconstruction techniques. Bone defects arising due to the resection of tumors or non-union fractures can be treated with the various methods indicated, with the benefits and disadvantages of each technique outlined. (Vidal et al. 2020)	28
<b>Figure 2.14</b>	Metal implants for orthopaedic applications. (Wu et al. 2021)	31

<b>Figure 2.15</b>	Intercalary reconstruction using segmental metal prosthesis (Zhao et al. 2020).	31
<b>Figure 2.16</b>	Processes involved in the manufacture of custom-made bone implants. (1) Bone CT scans are obtained for the patient. (2) Computer-aided software allows CT scans to be processed for (3) 3D printing customized constructs for (4) restoration of bone defects. In the bottom half, a genuine significant bone defect restoration process in metatarsal bone model of sheep is illustrated (Vidal et al. 2020).	32
<b>Figure 2.17</b>	Stress shielding in the proximal part of the femur due to bone-implant stiffness mismatch. Radiography compares the bone after 5 years of implantation (locations are highlighted) (Shanbhag and Rubash JJJ 2005).	34
<b>Figure 2.18</b>	A portion of solid hip implant is replaced with porous structure to avoid stress shielding and it's after effects (Limmahakhun et al. 2017).	36
<b>Figure 2.19</b>	Illustration of compressive stress-strain curve for porous structures (Maconachie et al. 2019).	38
<b>Figure 2.20</b>	Large bone defect: a multifaceted challenge. Bone healing is a complex process involving the interplay of many factors and well-orchestrated mechanisms.	39
<b>Figure 2.21</b>	Applications for porous materials (Banhart 2001).	40
<b>Figure 2.22</b>	Fully porous stem developed by a tetrahedron unit cell. (Moussa et al. 2018).	42
<b>Figure 2.23</b>	Classification of porous materials based on multiple factors.	43
<b>Figure 2.24</b>	Stochastic porous scaffolds (Murr et al. 2012). a) Foam based scaffold structure and b) Voronoi based scaffold structure Reprinted (adapted) with permission from (Wang et al. 2018).	44
<b>Figure 2.25</b>	Different unit cells of periodic porous structures showing a) BCC and its modified units, b) diamond unit cell, c) octet d) rhombic dodecahedron, e) rhombic cube octahedron, f) honeycomb unit cells, and g) TPMS based unit cells (Chen et al. 2020).	47
<b>Figure 2.26</b>	Nature inspired TPMS gyroid structure obtained from a) butterfly wings ( <i>Callophrys rubi</i> ), b) microscopic image of scales of <i>C. rubi</i> , c) magnified image of scales, d) CAD model of gyroid structure inspired from the wings of <i>C. rubi</i> . (Corkery and Tyrode 2017).	48
<b>Figure 2.27</b>	Illustration of the surface with constant mean curvature, representing the maximum and minimum curvatures ( $k_1$ and $k_2$ ) at a point on the surface.	49
<b>Figure 2.28</b>	Examples of different TPMS unit cells and their corresponding lattice structures (3x3x3 tessellations) where a) Schwarz Primitive, b) Schwarz Diamond, c) Schoen Gyroid, d) Schoen I-WP, e)	50

	Schoen F-Rhombic Dodecahedra (F-RD), and f) Fischer-Koch S (Al-Ketan and Abu Al-Rub 2019).	
<b>Figure 2.29</b>	Soap film used to produce minimal surface.	51
<b>Figure 2.30</b>	Bio-manufacturing process illustrated with a flowchart and detailed design strategy (Guddati et al. 2019).	55
<b>Figure 2.31</b>	Classification of additive technologies for developing porous structures.	56
<b>Figure 2.32</b>	(a) Schematic of Powder Bed Fusion process and (b) demonstration of the SLM technology.	56
<b>Figure 2.33</b>	The clinical application of common metal implants (Bai et al. 2019).	58
<b>Figure 3.1</b>	General methods for modeling porous structures.	70
<b>Figure 3.2</b>	Dual approach for modeling TPMS structures.	73
<b>Figure 3.3</b>	Representation of Gaussian map.	74
<b>Figure 3.4</b>	The Weierstrass representation and Bonnet transformation.	75
<b>Figure 3.5</b>	Flowchart illustrating the Marching Cubes algorithm.	78
<b>Figure 3.6</b>	Surface triangulation of a) Diamond b) Gyroid c) IWP and d) P structures.	79
<b>Figure 3.7</b>	Parallel surfaces centered on a unit cell of the gyroid Minimal surface.	80
<b>Figure 3.8</b>	Illustration of triangulated closed implicit surfaces for the gyroid structure.	81
<b>Figure 3.9</b>	Relation between volume fraction and the level set constant 'c'.	83
<b>Figure 3.10</b>	Disconnections of the implicit surface and their corresponding ranges.	83
<b>Figure 3.11</b>	Illustration of possible errors in the use of marching cube algorithm.	86
<b>Figure 3.12</b>	Methods for generating solid geometries.	87
<b>Figure 3.13</b>	NURBS resurfacing process for isolated regions of artefact. (A) Sharp edges are visible on the surface of segmented structures (black outlines) (B) NURBS (red curve) resurfaces the edges by integrating the control points. (C) The volumetric FEs are reduced by smooth surfaces.	90
<b>Figure 3.14</b>	Illustration of issues using CAPPED STL models.	91
<b>Figure 3.15</b>	Step sequence followed to develop solid model of unit cell from non-intersecting STL surface.	93

<b>Figure 3.16</b>	Process flow diagram for the conversion of TPMS STL data to multiscale CAD design.	94
<b>Figure 3.17</b>	Illustration of unit cell shape, size and strut thickness.	96
<b>Figure 3.18</b>	Estimation of maximum Von Mises stress of different sizes of unit cells on constant volume fraction and porosity.	96
<b>Figure 3.19</b>	Cubical space for the number of unit cell repetitions.	98
<b>Figure 3.20</b>	The effective Young's modulus of a finite model with a number of unit cells varying from 1 to 5 is predicted.	98
<b>Figure 3.21</b>	General view of typical closed TPMS models used in this work: from left to right D, G, IWP, and P surface, respectively (a) Unit Cell (b) Lattice Structure.	99
<b>Figure 4.1</b>	Designed porous structures with different level of porosity and different porosity types: a-f) Primitive; g-i) Gyroid; m-r) Diamond; s-x) IWP. For each set of porosity type, top structure is unit cell of $1 \times 1 \times 1$ mm and bottom are lattice structure which is pattern of unit cell in three coordinates having size of $2 \times 2 \times 2$ mm. And for each set of porosity type, viewing from right to left, the level of porosity varies with 10% of intervals from 40% to 90%. ( $V_f$ indicates the volume fraction which is opposite of porosity).	103
<b>Figure 4.2</b>	Illustration of porous volume ( $V_s$ ) and solid volume ( $V$ ).	104
<b>Figure 4.3</b>	TPMS unit cells with the pore size definition in which pore size are labelled by $p$ .	105
<b>Figure 4.4</b>	Illustration of thickness determination for TPMS structures.	106
<b>Figure 4.5</b>	Thickness of porous structures with different porosity levels.	109
<b>Figure 4.6</b>	Pore sizes of porous structures with different porosity levels.	110
<b>Figure 4.7</b>	Surface area to volume ratio of porous structures with different porosity levels.	111
<b>Figure 4.8</b>	Pore sizes of structures with varying thickness levels.	112
<b>Figure 4.9</b>	Surface area to volume ratio of structures with varying thickness levels.	112
<b>Figure 4.10</b>	Surface area to volume ratio of porous structures with different pore sizes.	113
<b>Figure 5.1</b>	Representative hexahedral meshing (a) Primitive, 80% Porosity (b) Gyroid, 80% Porosity.	120
<b>Figure 5.2</b>	Illustration of loading and boundary condition of lattice structures.	122
<b>Figure 5.3</b>	Illustration of Directional deformation from FEA simulation. TPMS models are Top-Left (D-Lattice), Top-Right (G-Lattice)	124

	Bottom-Left (IWP-Lattice), and Bottom-Right (P-Lattice) respectively, with identical loading conditions and material property for all lattices.	
<b>Figure 5.4</b>	Compressive Stress-Strain curve of four analyzed lattice structures with 90% porosity.	125
<b>Figure 5.5</b>	Demonstration of Effective Elastic Modulus ( $E_{eff}$ ) of D, G, IWP, and P lattice drawn from linear region fit of a straight line on the compressive stress-strain curve.	126
<b>Figure 5.6</b>	Reduced Elastic Modulus of solid Ti6Al4V on all four types of lattices	126
<b>Figure 5.7</b>	Compressive strength of all four types of lattices.	127
<b>Figure 5.8</b>	Illustration of Equivalent strain distribution at 409 N force of four TPMS lattice structures at porosity level of 70%.	129
<b>Figure 5.9</b>	Compressive Stress-Strain curve of four analyzed lattice structures with varying porosity level.	130
<b>Figure 5.10</b>	Reduced Young Modulus of solid Ti6Al4V on all four types of lattices for different porosity level	131
<b>Figure 5.11</b>	Compressive strength of scaffolds with varying porosity level.	132
<b>Figure 6.1</b>	Illustration of gyroid and primitive TPMS unit cells with varying volume fraction which is uniquely patterned in X, and Z coordinate to take desired shape of lattice or scaffold. An interpenetrating fluid phase is created by subtracting the solid volume with the volume of lattice. Similarly illustrated, primitive scaffold of varying volume fraction from 10% to 50% is included in this study.	140
<b>Figure 6.2</b>	Modelling domains represented as grey (solid) and pink (fluid) for (left) Gyroid and (middle) Primitive (right) Illustration of mesh for TPMS and fluid geometry.	141
<b>Figure 6.3</b>	Velocity vectors at inlet velocity of 0.1 mm/sec; left column is for gyroid and right is for primitive.	144
<b>Figure 6.4</b>	Pressure contour at inlet velocity of 0.1 mm/sec; left column is for gyroid and right is for primitive.	146
<b>Figure 6.5</b>	Variations in Wall Shear Stress with the change in porosity. left column is for gyroid and right column is for primitive.	149
<b>Figure 6.6</b>	Average WSS with a velocity of 0.1 mm/sec in all the models	151
<b>Figure 6.7</b>	Average permeability with 0.1 mm/sec velocity in total developed models.	152
<b>Figure 6.8</b>	Average WSS having 0.1 mm/sec velocity for total developed models on various thickness.	153
<b>Figure 6.9</b>	Average permeability having 0.1 mm/sec velocity for total developed models.	154

<b>Figure 7.1</b>	A) Boundary contour to detect bone region on the medical image (B) Search lines from each control points to control fit of contours converge to or diverge from the centre to predict the contour on the subsequent slices (Safont et al. 1999).	158
<b>Figure 7.2</b>	Illustration of the steps involved in the process of development of 3D model of femur and conversion of STL model to solid model.	160
<b>Figure 7.3</b>	Hounsfield scale showing a range of Hounsfield Unit for body system.	162
<b>Figure 7.4</b>	DICOM patient-based coordinate system	162
<b>Figure 7.5</b>	Schematic illustrating the process of data acquisition.	163
<b>Figure 7.6</b>	Clear distinction between a preset bone scale and a soft tissue scale is used to set the contrasts in Mimics 18.0 (Materialise, Leuven, Belgium)	164
<b>Figure 7.7</b>	Image showing bone scale volume rendered data.	165
<b>Figure 7.8</b>	CT images of femur bone are thresholded with Bone (CT) scale. (a) Axial (b) Coronal (c) Sagittal View.	168
<b>Figure 7.9</b>	Profile line graph illustrating the threshold range for bone (CT).	169
<b>Figure 7.10</b>	Illustration of the region grow process.	169
<b>Figure 7.11</b>	Effects of region grow followed by manual segmentation to develop accurate 3D model.	170
<b>Figure 7.12</b>	Illustration of 3D reconstruction process of femur bone in MIMICS software.	171
<b>Figure 7.13</b>	2D CT images converted to 3D model using Mimics Software.	172
<b>Figure 7.14</b>	Developed 3D model of femur bone structure.	172
<b>Figure 7.15</b>	Effect of smoothing on developed 3D model. (a) Rough surface with sharp edges, (b) Smooth surface with no sharp edges.	173
<b>Figure 7.16</b>	Porous scaffolds with complex internal structures and high-quality exterior interfaces (Yoo et al. 2011b).	175
<b>Figure 7.17</b>	Schematic representation of complete process involved in the development of patient specific scaffold to treat segmental bone defect.	176
<b>Figure 7.18</b>	Illustration of mesh generation a) Femur with solid scaffold a) Femur with anatomically matched P scaffold.	177
<b>Figure 7.19</b>	Typical views of construct (a) Femur critical size defect replaced with anatomically matched scaffold (b) Loading and boundary conditions on the construct.	180
<b>Figure 7.20</b>	Von mises stress distribution a) Femur with solid scaffold b) Femur with P scaffold.	181

<b>Figure 7.21</b>	Biomechanical setup of the critical size bone defect with solid and porous scaffolds on femur bone to demonstrate the stress transfer patterns (a). The femur bone defect replaced with P lattice structures with 80% porosity (top right shows the enlarged lateral view and bottom right shows the front view illustrating the defect where bone fragments have contact. (b) The femur bone defect replaced with solid scaffold. (c) Stress transmission pattern on the bone at P scaffold and bone interfaces after removing scaffold. (d) Stress transmission pattern on the bone at solid scaffold and bone interfaces after removing solid scaffold. (e) Von Mises stress patterns of bone with porous scaffold (Front view). (f) Von Mises stress patterns of bone with porous scaffold (Front view). A threshold of the maximum value of 50 MPa was set to visualize the stress concentration in the (g) Model with P scaffold and (h) Model with a solid scaffold.	183
<b>Figure 8.1</b>	Sequence of steps in prosthesis extraction accounting specific anatomy.	189
<b>Figure 8.2</b>	Conceptualization of prosthesis (a) 3D view (b) Section view (c) Exploded view.	189
<b>Figure 8.3</b>	Primitive unit cell mapped patient specific implant (a) Upper part illustrating length compensator mechanism to tolerate the micro mismatch of length of implant (b) Lower part of implant illustrating large bore tail and fins to provide resistance to bending and torsional load. (c) Anterior view of complete assembly (d) posterior view of complete assembly (e) 3D view of implanted assembly at anatomical location (thigh)	190

## LIST OF TABLES

Table No.	Table Description	Page No.
<b>Table 2.1</b>	Mechanical properties of cortical and cancellous bone (Dziaduszezwska and Zieliński 2021).	16
<b>Table 2.2</b>	Major requirements for load-bearing metallic biomaterials (Williams 2008).	58
<b>Table 2.3</b>	Mechanical properties of most common biomedical metal alloys (Li et al. 2014).	59
<b>Table 2.4</b>	Composition of Ti6Al4V (Grade 5) alloy in % wt (Breme et al. 2016).	59
<b>Table 2.5</b>	Material Properties of Ti6Al4V (Yánez et al. 2018).	60
<b>Table 3.1</b>	Nodal equations of some commonly used TPMS structures (Yoo 2011).	71
<b>Table 3.2</b>	Calculated level set constants for the volume fraction ranging from 50% to 10%.	84
<b>Table 4.1</b>	Estimated pore size of TPMS structures.	105
<b>Table 4.2</b>	Estimated thickness of TPMS structures.	106
<b>Table 4.3</b>	Estimated volumes and surface area of the structures and its calculated Surface-area-to-volume-ratio.	107
<b>Table 5.1</b>	Material Properties of Ti6Al4V (Yánez et al. 2018).	119
<b>Table 5.2</b>	Calculated Effective Elastic Modulus ( $E_{eff}$ ) of D, G, IWP, and P.	126
<b>Table 5.3</b>	Calculated Effective Elastic Modulus ( $E_{eff}$ ) of D, G, IWP, and P at different porosity level.	131
<b>Table 5.4</b>	Mechanical properties of various porous structures modelled with different materials.	134
<b>Table 6.1</b>	Number of elements generated in each structure.	143
<b>Table 7.1</b>	A range of predefined Grayscale with maximum and minimum values.	165
<b>Table 7.2</b>	Number of elements and nodes generated in each component of the model for finite element analysis.	178

<b>Table 7.3</b>	Adopted orthotropic material properties for finite element of femur construct.	178
<b>Table 7.4</b>	Applied loads on the model.	179

Musculoskeletal disorders and associated bone diseases are one of the major causes of pain and disability, resulting in a social and economic burden for our society. Due to the rapidly changing lifestyles of individuals, orthopedic conditions are considered to be the most affected. Joint diseases, like osteoarthritis and rheumatoid arthritis; bone diseases, like osteoporosis and consequent fragility fractures and trauma-related fractures; bone tumors i.e. osteosarcoma, frequently observed at the physis of the bones often lead to the problem of large segmental bone defects (LSBD). These are severe injuries affecting individuals of all generations causing continuous discomfort that limits motion, flexibility, and complete functional strength, significantly decreasing work efficiency and making their treatment and outcomes difficult. Limb ablation was formerly the only acceptable means for attaining disease eradication. Restoration and joint preservation for high-risk patients suffering from significant traumatic bone injuries continue to be a major problem of orthopedics. When the joint function is impaired or bone defects are too large to be treated with bone grafts, prosthetic implants are the gold standard to replace the defective location or fill the gap.

Engineering and medical technology breakthroughs in recent years have offered the resources to design and implement novel medical methods to overcome these challenges. However, despite the tremendous progress in the field of orthopedic implant devices (material and design), a reasonable proportion of patients undergoing bone reconstruction or limb salvage surgery with conventional/standard metal prosthetics are continuously experiencing a variety of postoperative complications which compromises the overall outcomes causing residual pain due to these off-the-shelf implants. Pathophysiologic, mechanical, or a combination of both conditions are responsible for such complications, due to which the developed implants are still not completely marked as optimum. However,

the long-term success of a prosthesis is directly or indirectly dependent on the biomaterials used and the shape of the prosthesis. To date, medical-grade titanium and its alloys (Ti6Al4V) are considered one of the most biocompatible metals and are used to fabricate implants due to their outstanding outcomes and long-term stability. However, due to its high elastic modulus of  $\approx 110$  GPa as compared to natural bone ( $\approx 0.02$ -30 GPa), stiffness mismatch between bone and implant results in the stress-shielding phenomena. It occurs due to inefficient stress transfer to the bone surrounding the implant causing bone weakening and implant loosening thereby resulting in the ultimate failure of the implant. Additionally, conventional fabrication methods such as gas injection molding, hot isostatic pressing, etc. are used to provide porous coatings on the implant surface to enhance the biological properties. These coatings are simply made up of arbitrarily distributed and shaped pores with uncontrolled sizes, making it difficult to achieve quantitatively adjusted stiffness around the bone anatomy and no possibility of bone ingrowth and nutrient transport. Hence, these traditional implants are not sufficient for generating complex geometrical cellular structures that can vary the strength of Ti6Al4V implants to mimic the natural bone properties. Furthermore, due to the dynamic variability of bone structure, the traditionally manufactured implants used for the treatment of SBD usually lead to maladaptation resulting in the ultimate failure of the prosthesis in the postoperative period. To address these issues, the present study focuses on the computational design and development of patient-specific porous implants inspired by advanced additive manufacturing (3D printing) techniques that can provide the advantages of customized fit being patient-specific (PS) in nature; lightweight porous geometry enables better mechanical performance by reducing stiffness gap between bone and implant and facilitates the possibility of bone ingrowth thereby being permeable to body fluids and nutrient exchange. The global objective of this research is to computationally analyze and evaluate

the morphological, mechanical, and permeable performance characteristics of the designed and developed porous structures for the treatment of large segmental bone defects. The porous implant geometry is typically based on the nature-inspired triply periodic minimal surfaces (TPMS), which have unique properties of sustaining extensive loads with extremely lightweight geometry.

The study includes four sequential stages. First stage deals with the efficient mathematical modeling and design of TPMS-based porous structures which are parameterized for robustness. The selection criterion for TPMS structures specifically, Schwarz primitive (P) and diamond (D), and Schoen's gyroid (G) and I-graph wrapped package (IWP), included in this research work are based on previous in vivo studies on the effect of shape and size of porous structures. The effect of morphological parameters like thickness constant on volume fraction; the size of a unit cell on stress distribution; pore size, as well as the effect of the number of unit cells on the change in elastic modulus of TPMS structures is evaluated to select an optimum criterion for the study of lattice TPMS structures that uniquely patterned in three coordinates. Based on this criterion, robust analytical (implicit) and CAD-based modeling approaches are employed to obtain an optimized unit cell structure that can be effectively used for FEA purposes. An algorithm to convert the STL model into a solid model is developed that enables easy implementation of these models for finite element studies (FEA). TPMS lattices for each of the P, D, G, and IWP structures are then modeled by repeating the unit cells in three independent (x, y, and z) Cartesian coordinates. At the end of this stage, four TPMS lattice structures of 2x2x2 are obtained to evaluate the mechanical performance for their possible applications depending on the bone quality of the application area.

The second stage deals with the preparation of FE models of the TPMS lattice structures for evaluating the morphological properties such as thickness, pore size porosity, and

surface-to-volume ratio to assess the suitability of structures for bone replacement accounting for cell adhesion, migration, and bone ingrowth. The mechanical performances of these lattices were numerically analyzed by assigning additively manufactured Ti6Al4V nonlinear material properties and applying boundary conditions with appropriate meshing parameters and loading steps in accordance with ISO 13314:2011. This enables the establishment of a unique structural-mechanical relationship for the structures included in this study. The assessment was done to study the effect of the design, pore size, porosity, and strut thickness on the mechanical, and morphological properties of these structures. Finite element structural analysis was performed to study the stress distribution pattern, elastic modulus, compressive strength, and energy absorption properties to assess the mechanical performance characteristics of TPMS lattice structures. Additionally, computational fluid dynamics (CFD) analysis was also performed to study the mass-transport properties such as permeability, and wall shear stress (WSS) of the fluid, to assess the vascularization and cell attachment thresholds on the following parameters included in the mechanical evaluation.

The third stage demonstrates the development of a 3D femur model obtained from CT scan data of healthy femur bone providing key insights into anatomical features. The developed 3D femur model was used to create an intentional segmental bone defect of 50 mm size that was surgically fixed with a TPMS-based (P) porous scaffold of 80% porosity, to assess the performance on account of stress shielding. The porous scaffold is implanted at the defect location and physiological boundary conditions are applied to the assembly to study the stress transfer pattern from the implant to surrounding bone tissue.

Lastly, the fourth and final stage deals with the development of patient-specific prostheses to treat tumor-infected femur bone. Surgical resection of the tumor-infected segmental defect was performed virtually and a morphologically controlled PS prosthesis particularly

signifying large segmental bone defects was developed with the conceptualization of the insertion of the implant to the final outcomes. To this, a complete strategy was demonstrated to develop a conceptual prosthesis enabling porous structures with controlled morphological features that mimic the host bone. Lastly, the approach of porous mapping on the solid implant is well represented which helps to obtain an anatomically matched lightweight structure to bridge the gap between the mechanical performances and ultimate outcomes of the treatment of large segmental bone defects.

Overall, the results indicated that the TPMS-based porous structures have the potential to be used as porous scaffolds for the treatment of large segmental bone defects in orthopedic applications. Due to their outstanding load-bearing abilities with extremely lightweight geometry and dynamically variable morphological and mechanical properties, the TPMS-based porous scaffolds fabricated with Ti6Al4V inspired by additive manufacturing technology can be applied at different anatomical locations of bone depending on the bone quality. Also, the novel concept of anatomically matched porous implant design presents its potential to be used in the real scenario of applications in orthopaedics subjected to experimental and clinical validations.